

**Probing thermal magnon current
mediated by coherent magnon
via nitrogen-vacancy centers in diamond**

Dwi Prananto^{1*†}, Yuta Kainuma¹, Kunitaka Hayashi¹, Norikazu Mizuochi²,

Ken-ichi Uchida^{3, 4, 5}, Toshu An^{1‡}

¹School of Materials Science, Japan Advanced Institute of Science and Technology,

Nomi, Ishikawa 923-1292, Japan

²Institute for Chemical Research, Kyoto University, Gokasho, Uji, Kyoto 611-0011,

Japan

³National Institute for Materials Science, Tsukuba 305-0047, Japan

⁴ Institute for Materials Research, Tohoku University, Sendai 980-8577, Japan

⁵Center for Spintronics Research Network, Tohoku University, Sendai 980-8577, Japan

*e-mail: prananto@jaist.ac.jp

† Present address: Materials Science Program, Faculty of Engineering, Niigata University, Niigata City, Niigata 950-2181, Japan

‡e-mail: toshuan@jaist.ac.jp

Currently, thermally excited magnons are being intensively investigated owing to their potential in computing devices and thermoelectric conversion technologies. We report the detection of thermal magnon current propagating in a magnetic insulator yttrium iron garnet under a temperature gradient, using electron spins associated with nitrogen-vacancy (NV) centers in diamond. By exploiting the interplay between coherent and incoherent magnons, thermal magnon current is observed via NV spins hosted in a beam-shaped bulk diamond and a nanodiamond coupled with coherent magnon in the form of modified Rabi oscillation frequencies as well as spin relaxation rates. The local probing of thermal magnon current serves as a basis for creating a new device platform hybridizing spin caloritronics and spin qubits.

Introduction

The utilization of magnons, i.e., the quanta of collective excitation of spins, in a magnetically ordered media for transmitting and processing information has flourished in the recent decade and is known as magnon spintronics¹⁻⁴. Moreover, the emerging field of spin caloritronics⁵, which utilizes the interplay between spin and heat currents,

resulted in an alternative strategy in creating more efficient computing devices^{6,7} and versatile thermoelectric conversion technologies⁸.

Quantum sensors based on the electron spins associated with nitrogen-vacancy (NV) centers in diamond has been regarded as high-resolution and high-sensitivity sensors for various condensed matter phenomena^{9,10,11}. NV centers can be strongly coupled with coherent magnetostatic spin waves (MSWs) owing to their energy matching (one to tens of gigahertz)¹²⁻¹⁸. Thermally excited magnons, which appear in a significantly higher energy regime (defined by $\hbar\omega = k_B T$) than NV spins, are rarely investigated through NV spin-based magnetometry owing to the gap between their energies. These incoherent and high energy magnons are known to interact with lower-energy magnons (MSWs) by transferring their spin angular momentum, known as the thermal magnon spin-transfer torque¹⁹⁻²⁴.

Recently, magnon population has been measured and controlled via pumping the NV center by spin waves at the NV spin resonance frequencies with a single NV spin sensitivity²⁵⁻²⁷. Furthermore, the same effect was observed nonlocally using the inverse spin Hall effect²⁸. Additionally, NV spin excitations and modulations via the spin-

transfer-torque oscillation of spin waves by electrical methods through the spin Hall effect has been demonstrated recently^{29,30, 31}.

Herein, we report the detection of thermally excited magnon current mediated by coherent magnon (MSW) by exploiting the thermal magnon spin-transfer torque (Fig. 1), bridging the energy gap between the higher energy thermally excited magnon and the lesser energy NV spin. Using the NV spins hosted in a bulk single crystal and a nanocrystal diamond (nanodiamond), we observed the modification of the magnetostatic surface spin waves (MSSWs') magnetization dynamics under the influence of the thermal magnon current applied to a magnetic insulator yttrium iron garnet (YIG) sample.

Results

System and experimental procedure

We used a liquid-phase-epitaxy grown YIG sample in the form of a trilayer of single-crystalline YIG/gadolinium gallium garnet (GGG)/YIG of thicknesses 100, 550, and 100 μm , respectively, measuring 6 mm \times 3 mm (Fig. 2a). To improve the lattice

matching between YIG and GGG, a small amount of yttrium in the YIG was substituted with bismuth.

Throughout the experiment, external magnetic fields $\pm B_{\text{ext}}$ were applied along the y-axis with a tilted angle ϕ to the surface plane of the YIG/GGG/YIG (Fig. 2a). Two gold-wires antenna A and B (50 μm in diameter) were overlaid on the surface near both edges of the upper YIG, separated approximately 2 mm away to excite MSSWs by electrical microwave field, and the MSSWs propagates along the $\mathbf{k} \parallel \mathbf{B}_{\text{ext}} \times \hat{\mathbf{n}}$ direction ($\hat{\mathbf{n}}$ is a vector normal to the YIG's surface) unidirectionally³². In this experimental setup, the MSSWs are predominantly excited on the upper YIG layer surface by one of the antenna and propagate to the other end of the sample depending on the polarity of the applied external magnetic field; $+B_{\text{ext}}$ ($-B_{\text{ext}}$) along with the $+y$ ($-y$) axis (Fig. 2a shows the case for antenna A excitation).

We used two types of diamond to host the NV centers as a quantum sensor for the detection of thermally excited magnons; a diamond beam ((110) oriented) measuring 2.5 mm \times 0.1 mm \times 0.1 mm containing a layer of the NV spin ensemble and a nanodiamond of diameter approximately 40 nm containing several NV spins (adamas nano). It is noteworthy that the use of the diamond-beam with a known NV axis

direction is suitable for efficient resonant NV spin excitations but not for non-resonant excitations owing to the significant distance of approximately $1\text{ }\mu\text{m}$ separating the NV spins and the YIG surface¹⁸. Meanwhile, the use of nanodiamonds with an unknown NV axis is not suitable for efficient resonant NV spin excitations but suitable for non-resonant excitations because of their proximity to the YIG surface³³.

As shown in Fig. 2a, the diamond beam was placed on the upper YIG's layer at the middle of its longitudinal direction, where an external magnetic field $+B_{\text{ext}}$ directed along the y-axis ($[00\bar{1}]$ crystal direction of the diamond beam) creates an angle ϕ of 32° to the (110) plane (157° to NV3 ($\parallel [111]$)) of the diamond beam (Fig. 2a). This setup separates the resonance transitions of the four possible NV spins directing to the $\langle 111 \rangle$ symmetrical axes (NV1 $\parallel [1\bar{1}\bar{1}]$, NV2 $\parallel [\bar{1}1\bar{1}]$, NV3 $\parallel [111]$, and NV4 $\parallel [\bar{1}\bar{1}1]$). A small tilt angle of less than 1 degree between $+B_{\text{ext}}$ and $[00\bar{1}]$ separates the NV1 and NV2 resonance transitions. The angles used were determined by the fitting of optically detected magnetic resonance (ODMR) spectra mapping of NVs (not shown here).

A temperature gradient was created along the longitudinal direction in the YIG sample by increasing or lowering the temperature at either site A (T_A) or site B (T_B). Such

temperature control keeps the temperature at the middle of the YIG's longitudinal dimension constant, as well as the diamond beam's temperature owing to its high thermal conductivity, under the application of temperature difference ΔT up to 10 K (Fig. 2a). This was confirmed using the temperature sensing capability of the NV spins³⁴⁻³⁶ (see Supplementary Note 4). ΔT is defined as the difference between T_A and T_B ($\Delta T = T_A - T_B$).

For ODMR measurements, the NV spins' ground triplet (3A_2) states, $m_s = 0$ and $m_s = \pm 1$, are optically addressed using an in-house scanning confocal microscope (see Supplementary Note 2). The spin-state selective photoluminescence (PL) nature of the NV spin allows us to optically discriminate the spin qubit states (the $m_s = 0$ yields a higher PL than the $m_s = \pm 1$). In this study, spin-state manipulation, $m_s = 0 \leftrightarrow \pm 1$, was performed by the MSSWs-generated electromagnetic microwave radiation (Fig. 2b), propagated from one of the gold-wire antenna to the laser spot position separated approximately 1 mm away^{15,16}.

Spin wave and NV spin resonance mapping

The MSSWs were excited from antenna A with microwave (MW) power $P_{MW} = 1$ mW in an increasing external magnetic field $+B_{ext}$, and the YIG's global coherent spin-

waves resonance spectra were mapped out by performing microwave absorption (S_{11} -parameter) measurement using a vector network analyzer (Rohde & Schwartz ZVB8) at zero temperature difference. Figure 2c shows a map of the spin-wave spectra, exhibiting lines of resonance of the MSSWs spanning to the higher frequencies from the uniform Kittel mode (ferromagnetic resonance (FMR)). The solid red and yellow lines indicate the NV spins' upper ($m_s = 0 \leftrightarrow +1$) and lower ($m_s = 0 \leftrightarrow -1$) bound resonance transitions defined by the Zeeman energy, respectively¹⁶. When an energy matching condition between the MSSW and NV spins is fulfilled ($f_{\text{MSSW}} = f_{\text{NV}}$), the NV spins can be coherently excited by the MSSW^{15, 16}. From the result in Fig. 2c, we can expect excitations of the NV spins by the MSSWs within the frequencies spanning between the red and yellow lines.

Next, we mapped out the MSSWs-driven NV spins resonance frequencies by performing ODMR spectroscopy with an increasing external magnetic field $+B_{\text{ext}}$ at zero temperature difference using the diamond beam. Figure 2d shows a color map of the MSSWs-driven electron spin resonance from an ensemble of NV spins in the diamond beam. As expected, only the NV spins' resonance transitions that matched with the MSSW's resonance frequencies underwent a PL intensity quenching as a

consequence of the transition from $m_s = 0$ to $m_s = \pm 1$ ^{15,16}. In Fig. 2d, only the $m_s = 0 \leftrightarrow -1$ transitions that overlapped with the MSSW's resonance frequencies appeared. Furthermore, by zooming in around the NV3 spectral line in Fig. 2d, a discretized and broadened resonance line owing to the frequency matching between the NV spins and the different MSSW modes (Fig. 2e) was observed (Fig. 2f)^{17,37}. The spectra at a matching condition with $+B_{\text{ext}} = 19$ mT, $f_{\text{MW}} = 2.58$ GHz between one of the MSSW modes and the NV spins are shown in Figs. 2g and h.

Detection of thermal magnon current via coherent driving of NV spins

In a magnet under a temperature gradient, thermal magnon current is generated and exerts a thermal spin-transfer torque τ_{tm} to precessing magnetization of coherently excited MSSWs (Figs. 1 and 2b). The phenomenon has been well known to be detected by electrical way through microwave response (Yu et al.²⁴) and the inverse spin Hall effect^{21,22,23}. Here an ensemble of NV spins in the diamond beam is utilized to detect the thermal magnon current mediated by MSSWs (Figs. 2a, b). Note that the applied magnetic field is perpendicular to the MSSWs propagation and the temperature gradient direction (Fig. 2a), different from that of Yu et al.'s setup (parallel) and the inverse spin Hall effect cannot be used.

First, the ODMR spectra of the NV spins excited by the MSSW were analyzed under a temperature gradient. We tuned the resonance frequency to one of the matching condition frequencies of 2.58 GHz as shown in Figs. 2g, h and analyzed the PL contrast of the ODMR as the temperature difference ΔT varied. In Figure 3a, the ODMR spectra with resonance dips at 2.58 GHz ($+B_{\text{ext}} = 19$ mT, $P_{\text{MW}} = 1$ mW) are shown with increasing ΔT (-10 to 10 K). The ODMR's PL contrast is enhanced as ΔT evolved from positive to negative, though the MSSWs is driven by the same MW power $P_{\text{MW}} = 1$ mW. Their intensities were plotted together with linear fitting in Fig. 3b. This indicates a change in the amplitude of microwave AC field from the MSSWs³⁸, as thermal magnon current was generated under the application of temperature gradient in the upper layer of the YIG.

Next, we drove the NV spins into the Rabi oscillations between the qubit states of $m_s = 0$ and $m_s = -1$ via the MSSW-driven pulse sequence shown in Fig. 3c with the same matching condition of 2.58 GHz between the qubit states of $m_s = 0$ and $m_s = -1$ (Fig. 3d). The frequency of the Rabi oscillation Ω_R is proportional to the amplitude of the MSSWs oscillating driving field b_1 ($\Omega_R \propto b_1$) in the YIG sample³⁹ and hence can be used to detect the change in the MSSW's magnetization dynamics^{15,16}.

Hereafter, the Rabi frequency was enhanced as ΔT progressed from 0 to -10 K and was suppressed as ΔT progressed from 0 to $+10$ K (Figs. 3d and e). This is explained by the change of polarity of the thermal magnon spin-transfer torque²⁴ (Fig. 1). The Rabi field b_R ; electromagnetic field at the NV position above the YIG surface (Fig. 2b), can be estimated from the Rabi frequency through the relation $b_R = \Omega_R / \gamma_e$ ^{12,39,40}, with $\gamma_e = 2\pi \cdot 28$ GHz/T being the gyromagnetic ratio of electrons. The Rabi field b_R evolved from 19 ± 0.5 μ T at $\Delta T = 10$ K to 26 ± 0.4 μ T at $\Delta T = -10$ K, based on its plot as a function of ΔT (Fig. 3f); indicating a change of approximately 18 ± 1 % from 22 μ T at $\Delta T = 0$.

The unidirectional propagation of the MSSWs is inverted according to $\mathbf{k} \parallel \mathbf{B}_{\text{ext}} \times \hat{\mathbf{n}}$ ^{41,42} by applying different polarity of B_{ext} at the upper YIG surface and in this condition the thermal spin-transfer torque is applied with different polarity²⁴. Hence, we can expect to observe the same effect but with an inverted sign when we switch the external magnetic field to the $-y$ axis (assigned as $-B_{\text{ext}}$) and launch the MSSWs from the antenna B²⁴. We tuned the NV resonance frequency to a matching condition of 2.60 GHz ($-B_{\text{ext}} = 19$ mT, $P_{\text{MW}} = 1$ mW). As expected, the Rabi frequency was suppressed as ΔT progressed from 0 to -10 K and was enhanced as ΔT progressed from 0 to $+10$

K (Figs. 3g and h). In this geometry, the Rabi field is estimated to evolve from approximately $18 \pm 0.6 \mu\text{T}$ at $\Delta T = -10 \text{ K}$ to approximately $22 \pm 0.3 \mu\text{T}$ at $\Delta T = 10 \text{ K}$ (Fig. 3i); indicating a change of approximately $16 \pm 2 \%$ from $19 \mu\text{T}$ at $\Delta T = 0$.

The observed value of Rabi field is not well symmetric as a function of temperature difference between different polarity of the applied external magnetic field ($+B_{\text{ext}}$ and $-B_{\text{ext}}$). This may come from the imperfection of symmetry of the experimental setup due to the tilting angle formed between B_{ext} and the surface plane of the YIG, which affects the excitation amplitude of the MSSWs and intensity of the thermal magnon spin-transfer torque.

The observed effect can be interpreted as a thermal magnon spin-transfer torque τ_{tm} via the thermal magnon current generated by a temperature gradient^{4,43,44}, which interacts with the MSSW and relaxes by transferring its spin angular momentum. The transfer of spin angular momentum contributes to the development of an anti-damping torque τ_{tm} , which alters the MSSW's magnetization dynamics^{19,20,24} and perceived by the NV spins as an altering Rabi field strength (Fig. 1).

The effect can be described phenomenologically by the Landau–Lifshitz–Gilbert equation of magnetization dynamics with an additional term coming from the anti-damping torque induced by the thermal magnon current, as follows:²⁴

$$\frac{d\mathbf{M}}{dt} = \gamma_e(\mathbf{M} \times \mathbf{B}_{\text{eff}}) + \frac{\alpha_l}{M_s} \left(\mathbf{M} \times \frac{d\mathbf{M}}{dt} \right) + \gamma_e \boldsymbol{\tau}_{tm}, \quad (1)$$

where \mathbf{M} is the magnetization of the YIG, \mathbf{B}_{eff} is the effective magnetic field, α_l is the intrinsic Gilbert damping parameter of the magnetization dynamics, and $\boldsymbol{\tau}_{tm}$ is the anti-damping torque induced by the thermal magnon current defined by²⁴

$$\boldsymbol{\tau}_{tm} = \alpha_{tm} \frac{\omega_r}{|\gamma_e| M_s^2} \mathbf{M} \times (\mathbf{M} \times \mathbf{m}). \quad (2)$$

α_{tm} , ω_r , and \mathbf{m} are the thermal magnon torque damping parameter, resonance frequency of the spin wave, and transverse component of the magnetization precession, respectively (Figs. 1 and 2b). Here, the thermal magnon damping parameter is proportional to the temperature gradient applied to the YIG (see Supplementary Note 7 for the derivation)

$$\alpha_{tm} = - \left(\frac{\omega_r + \omega_0}{\omega_r} \right) \left| \frac{1}{M_s} \frac{dM_s}{dT} \right| \frac{1}{k} \nabla T, \quad (3)$$

with $\omega_0 = \gamma_e B_{\text{ext}}$, and M_s is the saturation magnetization of the YIG.

The relation between the Rabi field and temperature gradient can be inferred by analyzing the schematic toy model shown in Fig. 2b. The system is seen as a precessing magnetization with a small cone angle defined as $\theta = 2b_{\text{MW}}/\sqrt{3}\Delta B$ ⁴⁵. With b_{MW} is the microwave field driving the spin waves and ΔB is the spin wave resonance linewidth. Hence, the transverse component of the magnetization is given by $m = M_s \sin\left(\frac{2b_{\text{MW}}}{\sqrt{3}\Delta B}\right) \approx M_s \frac{2b_{\text{MW}}}{\sqrt{3}\Delta B}$. With the spin wave resonance linewidth $\Delta B = 2(\alpha_i + \alpha_{\text{tm}})\omega_r/\sqrt{3}\gamma_e$, the transverse component of the magnetization can be rewritten as a function of damping parameter $m \approx M_s \frac{\gamma_e b_{\text{MW}}}{(\alpha_i + \alpha_{\text{tm}})\omega_r}$. The Rabi field b_R that drives the NV spins to its Rabi oscillation is proportional to the transverse component of the magnetization precession with a factor related to the distance separating the NV spin and the upper YIG's surface^{17,30}

$$b_R \propto \lambda M_s \frac{\gamma_e b_{\text{MW}}}{(\alpha_i + \alpha_{\text{tm}})\omega_r} k e^{-kx} \quad (4)$$

Equation (4) is well fitted to the data in Figs. 3f and i using known values of $\alpha_i = 5 \times 10^{-3}$ (obtained from the linewidth of the spin wave resonance at $\Delta T = 0$, see Supplementary Note 6), $M_s = 1.2 \times 10^5$ A/m (obtained from the fitting of Kittel equation to the ferromagnetic resonance data in Fig. 2b), $k = 0.5$ rad/cm (obtained from the dispersion relation of surface spin wave $f_{\text{MSSW}} =$

$\sqrt{(\gamma_e B_0 + 4\pi\gamma_e M_s/2)^2 - (4\pi\gamma_e M_s/2)^2 \exp(-2kd)} / 2\pi^{46}$, $\omega_r = 2\pi \cdot 2.58$ GHz for $+B_{\text{ext}}$ and $2\pi \cdot 2.6$ GHz for $-B_{\text{ext}}$, and λ as a proportionality constant. Using a constant a that relate the thermal magnon damping parameter and temperature gradient (equation (3)) as a fitting parameter, the thermal magnon damping parameter α_{tm} was estimated to be $5.5 \pm 0.5 \times 10^{-4}$ for $+B_{\text{ext}}$ and $2.5 \pm 0.5 \times 10^{-4}$ for $-B_{\text{ext}}$ using an effective temperature difference of $\Delta T_{\text{eff}} = 5.6$ K at $\Delta T = 10$ K at the YIG top surface.

We note that the MSSWs propagate on the upper YIG layer surface from an antenna to the center position, and the effect occurs within the half of the YIG's longitudinal direction. We performed a heat transfer simulation on the YIG and found that the effective temperature difference (ΔT_{eff}) is smaller than the applied temperature difference (see Supplementary Note 3). Then, $\nabla T_{\text{eff}} = 5.6$ K/mm is used for ∇T .

The damping parameter values from thermal magnon torque agreed well with those reported previously^{21–24}, confirming the existence and contribution of thermal magnon current in the evolution of MSSW magnetization dynamics^{19,20,24}. Furthermore, we confirmed our observation of the thermally excited magnon current electrically by analyzing the spin wave resonance linewidth from the absorption microwave signal

(S_{11}) (see Supplementary Note 6 for the experimental details and data). We found a good consistency between the electrical measurement and the optical measurement using the NV spins.

Local detection via non-resonant NV spin excitation

We extended the capability to detect the thermally excited magnon current locally via a small number of NV spins in a nanodiamond (Fig. 4a). The nanodiamonds were transferred to the middle of the YIG's longitudinal direction by dropping a small amount of nanodiamond solution with a micropipette. With the same setup and technique as in the experiment using the diamond beam, we mapped out the ODMR spectra of the NV spins in the nanodiamond to obtain information regarding the coupling between the MSSWs and the NV spins. Figure 4b shows the MSSW-driven ODMR spectral map exhibiting PL quenching at the resonance transition ($m_s = 0 \leftrightarrow -1$) of the NV spins together with PL image of the nanodiamond (inset) ($P_{\text{MW}} = 1$ W). Additionally, a strong non-resonant PL quenching was observed away from the NV spin transitions^{13,33} at frequencies from 2.5 to 2.7 GHz at the $+B_{\text{ext}}$ between 11.5 and 13.5 mT (Fig. 4b), where the MSSWs with high k -wave vectors was observed in Fig. 2c.

This non-resonant excitation is expected to change the longitudinal relaxation rate Γ of the optically polarized $m_s = 0$ state of the NV spins in the nanodiamond owing to its proximity to the surface of the YIG³³. The relaxation rate Γ can be inferred as the inverse of the time constant T_1 of the exponentially decaying population at $m_s = 0$. Under a perturbing dipolar field from a non-resonant MSSWs with a k -wave vector that matched with the inverse of the distance separating the NV spins and the YIG surface, the longitudinal relaxation rate Γ of the NV spins has been shown to increase, resulting in PL quenching^{12,25-27,47}. Recently, similar non-resonant effects were observed and attributed to PL quenching by parametric magnon excitation³³.

Based on the principle of the thermal magnon spin-transfer torque, we can expect the amplitude-modulation of the non-resonant MSSWs to alter the longitudinal relaxation rate Γ of the NV spins as a temperature gradient is applied to the YIG. We performed longitudinal spin relaxation measurement, in which the NV spins were polarized to $m_s = 0$ by the first laser pulse, followed by a dark time for duration τ before another laser pulse was applied to read the remaining population (Fig. 4c). By varying τ , the time-trace relaxation of the $m_s = 0$ state to its equilibrium state was observed. Under the application of temperature gradient ∇T to the YIG, MSSW at frequency of 2.66

GHz and $+B_{\text{ext}}$ and $-B_{\text{ext}} = 13$ mT (marked by dashed black circle in Fig. 5b) was driven with $P_{\text{MW}} = 1$ W during time τ to perturb the relaxation process.

The longitudinal relaxation rate Γ is related to the AC magnetic field amplitude generated by the MSSW, as described by $\Gamma \sim \frac{\gamma_e^2}{2} |B_{\perp}|^2$, with $|B_{\perp}|^2$ is the AC magnetic field perpendicular to the NV's quantum axis¹². Using equation (4) to replace B_{\perp} , we can obtain an equation relating the longitudinal relaxation rate Γ and temperature gradient as

$$\Gamma \propto \frac{\gamma_e^2}{2} \left| \frac{\lambda M_s \gamma_e b_{\text{MW}}}{(\alpha_i + a \Delta T) \omega_r} k e^{-kx} \right|^2. \quad (5)$$

This equation is in accordance with the data in Figs. 4d and e that the AC magnetic field from the MSSWs evolved with the temperature difference originated from the thermal spin-transfer torque between the thermally excited magnon current and the MSSW, thereby affecting the longitudinal relaxation rate of the NV spins.

Figures 4d and e show Γ as a function of ΔT applied to the YIG for $+B_{\text{ext}}$ and $-B_{\text{ext}}$ external magnetic fields, respectively, and fitted with equation (5). We estimated the thermal magnon damping parameter α_{tm} based on the fitting to the equation (5) as $2.6 \pm 0.6 \times 10^{-4}$ for $+B_{\text{ext}}$ and $1.5 \pm 0.5 \times 10^{-4}$ for $-B_{\text{ext}}$, values that show a good agreement with those estimated from the Rabi oscillation experiments. The

observed Γ at different polarity of external fields shows a symmetric trend owing to the non-reciprocal nature of MSSWs, though the values are not perfectly symmetric again as also seen in Figs. 3f and i due to the imperfection in the symmetrical excitations of the MSSWs and the thermal magnon spin-transfer torque.

Additionally, we performed a control experiment in which spin relaxation measurement was performed without driving a MSSW (Fig. 4f). The results in Figs. 4g and h show no dependence of spin relaxation rates on temperature difference (both graphs are plotted with the same y-axis scale as Figs. 4d and e, respectively). The results indicate that: 1) the energy of the thermally excited magnons is beyond the detection capability of the NV spins; therefore, they cannot directly be detected by the NV spins. 2) The MSSW is important as a mediator for the NV spins to detect the thermally excited magnon currents.

Discussion

We demonstrated the detection of thermally excited magnon currents mediated by coherent magnons of MSSWs via NV spins, where the thermal magnon spin-transfer torque emanated from the thermal magnon current altered the magnetostatic spin-

waves' magnetization precession when the YIG magnetic sample was subjected to a temperature gradient. The modulation of the magnetization dynamics of the MSSWs was perceived by the NV spins through the alteration of the Rabi oscillation frequency with the resonant NV spin excitation using a beam-shaped bulk diamond as well as the longitudinal spin relaxation rate with the non-resonant NV spins excitation using a nanodiamond.

This study provides a novel detection tool for thermal magnon currents via NV centers, which can be located locally and in a broad range of distances to spin waves. This feature cannot be obtained if only conventional methods, such as electrical detection via the inverse spin Hall effect, is used to investigate magnon dynamics, as the conventional method requires a relatively large electrode and specific configurations with proximal distance to the spin waves. Owing to the NV spin's single spin detection sensitivity enabled by its atomic-scale size⁴⁸, nanoscale probing and imaging of thermal magnon dynamics can be realized in the future, which can provide insights into novel practical applications in spin caloritronics and magnon spintronics^{12,17,29}.

Furthermore, the observed effect demonstrated the control of the NV spin quantum state by thermal magnons, mediated by the MSSWs. This introduces the potential application

of a novel hybrid quantum information processing system⁴⁹, where distant NV spins are bridged by a ferromagnet and can be coherently mediated and controlled via spin waves and thermal magnons to produce entanglements over long distances under ambient conditions^{15,16,30}.

Method

Diamond beam fabrication

We used a diamond with (110) crystal orientation fabricated via chemical vapor deposition by EDP Corporation. NV defects were created in the diamond by implanting $^{14}\text{N}^+$ ions using the ion source facility at the Japan Advanced Institute of Science and Technology, Center for Nano Materials and Technology with an implantation energy of 30 keV and a dose of 1×10^{12} ions/cm². The implantation was followed by annealing at 900 °C for 2 h to mobilize the vacancies to pair with the nitrogen atoms. Using Monte Carlo simulations with the stopping ranges of ions in matter software package⁵⁰, we estimated that the NV defects layer was distributed at the depth of approximately 33 nm beneath the diamond surface with concentration of about 0.6 ppm (substrate density of 3.52 g/cm³ and displacement energy of 37.5 eV^{51,52}). The

diamond was polished and cut into a diamond beam measuring $2.5\text{ mm} \times 0.1\text{ mm} \times 0.1\text{ mm}$ by Syntek Co., Ltd (see Supplementary Note 1).

Measurement setup

Optical measurements were conducted under an ambient environment using an in-house scanning confocal microscope (see Supplementary Figure 2). Optical excitation was performed using a 532 nm laser (MGL-III-532-20mW Changchun New Industries Optoelectronics Technology Co., Ltd.) focused onto an acousto-optical modulator (AOM) (Isomet 1250C) to provide a controlled pulse excitation with 1 mW of incident power at the sample. The laser was guided through optical lines to a $50\times$, NA = 0.6 objective lens (Nikon TU Plan ELWD). The emitted PL was filtered using a high-pass filter (Semrock BLP01-635R-25) before it was focused and coupled with a single-mode optical fiber and conveyed to a single photon counter module (SPCM) (Perkin Elmer SPCM-ARQH-14FC). The PL was integrated over a duration of 250 ns. Laser spot positioning on the sample and PL imaging were performed via a three-axis piezo nanopositioner (MCL nano-LP 100).

A microwave generator (DS Instruments SG6000F) was used to provide microwaves to excite the MSSWs delivered to the diamond. A high-speed multichannel pulse generator

(SpinCore Pulse Blaster PBESR-PRO-500) provided transistor–transistor logic signals to the AOM, RF switch (Minicircuit ZYSWA-2-50DR), and SPCM counter gate. A pair of electromagnet was used to provide an external magnetic field to split the NV spin degeneracy and magnetize the YIG.

To create a temperature gradient in the YIG, two Peltier modules (European Thermodynamics Limited ET-007-05-15) were used in the experiment. Each Peltier module was sandwiched between two aluminum plates; the bottom side of the Peltier modules was thermally connected to a large plate of room-temperature bath, and the upper side of the Peltier modules were thermally connected to hot/cold plates on which the YIG was bridged along the gap of 1 mm (see Supplementary Figure 3). The temperatures of both plates were measured using two T-type thermocouples connected to a dual-channel nanovoltmeter (Keithley 2182A), which provide feedback signals to control two source-meter instruments (ADCMT 6240A) that feed the Peltier modules. A proportional-integral-derivative control algorithm was applied to control the temperature difference between both ends of the YIG.

Data Availability

The data that support the findings of this study are available from the corresponding authors upon reasonable request.

References

1. Chumak, A. V., Vasyuchka, V. I., Serga, A. A. & Hillebrands, B. Magnon spintronics. *Nat. Phys.* **11**, 453-461 (2015).
2. Kajiwar, Y. et al. Transmission of electrical signals by spin-wave interconversion in a magnetic insulator. *Nature* **464**, 262-266 (2010).
3. Cornelissen, L. J., Liu, J., Youssef, J. B. & van Wees, B. J. Long-distance transport of magnon spin information in a magnetic insulator at room temperature. *Nat. Phys.* **11**, 1022-1026 (2015).
4. Giles, B. L., Yang, Z., Jamison, J. S. & Myers, R. C. Long-range pure magnon spin diffusion observed in a nonlocal spin-Seebeck geometry. *Phys. Rev. B* **92**, 224415 (2015).
5. Bauer, G. E. W., Saitoh, E. & van Wees, B. J. Spin caloritronics. *Nat. Mater.* **11**, 391-399 (2012).
6. Cornelissen, L. J., Liu, J., van Wees, B. J. & Duine, R. A. Spin-current-controlled modulation of the magnon spin conductance in a three-terminal magnon transistor. *Phys. Rev. Lett.* **120**, 097702 (2018).
7. Wu, H. et al. Magnon valve effect between two magnetic insulators. *Phys. Rev. Lett.* **120**, 097205 (2018).
8. Uchida, K. et al. Observation of longitudinal spin-Seebeck effect in magnetic insulators. *Appl. Phys. Lett.* **97**, 172505 (2010).

9. Casola, F., van der Sar, T. & Yacoby, A. Probing condensed matter physics with magnetometry based on nitrogen-vacancy centers in diamond. *Nat. Rev. Mater.* **3**, 17088 (2018).
10. Herbschleb, E. D. et al. Ultra-long coherence times amongst room-temperature solid-state spins, *Nat. Commun.* **10**, 3766 (2019)
11. Abe, E. & Sasaki, K. Tutorial: Magnetic resonance with nitrogen-vacancy centers in diamond—microwave engineering, materials science, and magnetometry. *J. Appl. Phys.* **123**, 161101 (2018).
12. van der Sar, T., Casola, F., Walsworth, R. & Yacoby, A. Nanometre-scale probing of spin waves using single electron spins. *Nat. Commun.* **6**, 7886 (2015).
13. Wolfe, C. S. et al. Off-resonance manipulation of spins in diamond via precessing magnetization of a proximal ferromagnet. *Phys. Rev. B* **89**, 180406(R) (2014).
14. Wolfe, C. S. et al. Spatially resolved detection of complex ferromagnet dynamics using optically detected nitrogen-vacancy spins. *Appl. Phys. Lett.* **108**, 232409 (2016).
15. Andrich, P. et al. Long-range spin wave mediated control of defect qubits in nanodiamonds. *npj Quantum Inf.* **3**, 28 (2017).
16. Kikuchi, D. et al. Long-distance excitation of nitrogen-vacancy centers in diamond via surface spin waves. *Appl. Phys. Express* **10**, 103004 (2017).
17. Zhou, T. X. et al. A magnon scattering platform. Preprint at <https://arxiv.org/abs/2004.07763> (2020).
18. Bertelli, I. et al. Magnetic resonance imaging of spin-wave transport and interference in a magnetic insulator. *Sci. Adv.* **6**, eabd3556 (2020).
19. Bender, S. A. & Tserkovnyak, Y. Thermally driven spin torques in layered magnetic insulators. *Phys. Rev. B* **93**, 064418 (2016).
20. Flebus, B., Upadhyaya, P., Duine, R. A. & Tserkovnyak, Y. Local thermomagnonic torques in two-fluid spin dynamics. *Phys. Rev. B* **94**, 214428 (2016).

21. Liu, L., Sun, Y., Jantz, M. & Wu, M. Control of ferromagnetic relaxation in magnetic thin films through thermally induced interfacial spin transfer. *Phys. Rev. Lett.* **108**, 257202 (2012).
22. Kajiwara, Y. et al. Spin-relaxation modulation and spin-pumping control by transverse spin-wave spin current in $\text{Y}_3\text{Fe}_5\text{O}_{12}$. *Appl. Phys. Lett.* **103**, 052404 (2013).
23. Jungfleisch, M. B. et al. Heat-induced damping modification in yttrium iron garnet/platinum hetero-structures. *Appl. Phys. Lett.* **102**, 062417 (2013).
24. Yu, H. et al. Thermal spin torques in magnetic insulators. *Phys. Rev. B* **95**, 104432 (2017).
25. Du, C. et al. Control and local measurement of the spin chemical potential in a magnetic insulator. *Science* **357**, 195-198 (2017).
26. Labanowski, D. et al. Voltage-driven, local, and efficient excitation of nitrogen-vacancy centers in diamond. *Sci. Adv.* **4**, eaat6574 (2018).
27. Purser, C. M. et al. Spin wave detection by nitrogen-vacancy centers in diamond as a function of probe-sample separation. *Appl. Phys. Lett.* **116**, 202401 (2020).
28. Liu, J. et al. Microwave control of thermal-magnon spin transport. *Phys. Rev. B* **99**, 054420 (2019).
29. Solyom, A. et al. Probing a spin transfer controlled magnetic nanowire with a single nitrogen-vacancy spin in bulk diamond. *Nano Lett.* **18**, 6494-6499 (2018).
30. Wang, X. et al. Electrical control of coherent spin rotation of a single-spin qubit. *npj Quantum Inf.* **6**, 78 (2020).
31. Zhang, H. et al. Spin-torque oscillation in a magnetic insulator probed by a single-spin sensor. *Phys. Rev. B* **102**, 024404 (2020).
32. Eshbach, J. R. & Damon, R. W. Surface magnetostatic modes and surface spin waves. *Phys. Rev.* **118**, 1208 (1960).
33. Lee-Wong, E. et al. Nanoscale detection of magnon excitations with variable wavevectors through a quantum spin sensor. *Nano Lett.* **20**, 3284-3290 (2020).

34. Acosta, V. M. et al. Temperature dependence of the nitrogen-vacancy magnetic resonance in diamond. *Phys. Rev. Lett.* **104**, 070801 (2010).
35. Toyli, D. M. et al. Measurement and Control of Single Nitrogen-Vacancy Center Spins above 600 K. *Phys. Rev. X* **2**, 031001 (2012).
36. Fukami, M. et al. All-optical thermometry based on nitrogen-vacancy centers in nanodiamonds. *Phys. Rev. Appl.* **12**, 014042 (2019).
37. Mühlherr, C., Shkolnikov, V. O. & Burkard, G. Magnetic resonance in defect spins mediated by spin waves. *Phys. Rev. B* **99**, 195413 (2019).
38. Dreau, A. et al. Avoiding power broadening in optically detected magnetic resonance of single NV defects for enhanced dc magnetic field sensitivity. *Phys. Rev. B* **84**, 195204 (2011).
39. Wang, P. et al. High-resolution vector microwave magnetometry based on solid-state spins in diamond. *Nat. Commun.* **6**, 6631 (2015).
40. Hanson, R., Dobrovitski, V. V., Feiguin, A. E., Gywat, O. & Awschalom, D. D. Coherent dynamics of a single spin interacting with an adjustable spin bath. *Science* **320**, 352-355 (2008).
41. An, T. et al. Unidirectional spin-wave heat conveyer. *Nat. Mater.* **12**, 549-553 (2013).
42. Wong, K. L. et al. Unidirectional propagation of magnetostatic surface spin waves at a magnetic film surface. *Appl. Phys. Lett.* **105**, 232403 (2014).
43. Giles, B. L. et al. Thermally driven long-range spin currents in yttrium iron garnet due to intrinsic spin Seebeck effect. *Phys. Rev. B* **96**, 180412 (2017).
44. Shan, J. et al. Criteria for accurate determination of the magnon relaxation length from the nonlocal spin Seebeck effect. *Phys. Rev. B* **96**, 184427 (2017).
45. Czeschka, F. D. et al. Scaling behavior of the spin pumping effect in ferromagnet-platinum bilayers. *Phys. Rev. Lett.* **107**, 046601 (2011).
46. Serga, A. A., Chumak, A. V., & Hillebrand, B. YIG magnonics. *J. Phys. D: Appl. Phys.* **43**, 264002 (2015).

47. Page, M. R. et al. Optically detected ferromagnetic resonance in diverse ferromagnets via nitrogen vacancy centers in diamond. *J. Appl. Phys.* **126**, 124902 (2019).
48. Wrachtrup, J. & Finkler, A. Single spin magnetic resonance. *J. Magn. Reson.* **269**, 225–236 (2016).
49. Kurizki, G. et al. Quantum technologies with hybrid system. *Proc. Natl. Acad. Sci.* **112**, 3866–3873 (2015).
50. Ziegler, J. F. *The stopping and ranges of ions in matter*, <http://www.srim.org>.
51. Toyli, D. M., Weis, C. D., Fuchs, G. D., Schenkel, T. & Awschalom, D. D. Chip-scale nanofabrication of single spins and spin arrays in diamond. *Nano Lett.* **10**, 3168 (2010).
52. Koike, J., Parkin, D. M. & Mitchell, T. E. Displacement threshold energy for type IIa diamond. *Appl. Phys. Lett.* **60**, 1450 (1992).

Acknowledgments

We thank E. Abe for fruitful discussions. This study was supported in part by JSPS

KAKENHI (JP18H01868, 18H04289, and 19K15444), Japan, by JST CREST

(JPMJCR1875 and JPMJCR17I1), and by JST A-STEP (JPMJTM19AV), Japan. N.M.

acknowledges support from KAKENHI (15H05868), MEXT Q-LEAP

(JPMXS0118067395), Japan.

Author contributions

D.P. and T.A. conceived the experimental idea. D.P. designed and performed the experiments with support from Y.K. and K.H. K.U. provided the YIG sample. D.P., Y.K., N.M., and T.A. analyzed and discussed the data. D.P. and T.A. wrote the manuscript. All authors discussed the experimental results and commented on the manuscript.

Competing interests

The authors declare no competing interests.

Figure Legends

Figure 1| Mechanism of thermal magnon current detection via NV center. In a magnet, thermal magnon current is created by applying temperature gradient ∇T , exerting an anti-damping torque τ_{tm} (against the damping torque τ_d) to spin wave (coherent magnon)'s precessing magnetization \mathbf{M} excited by a microwave AC field. Then, information of the thermal magnon current can be probed by nitrogen-vacancy (NV) center spin in diamond near the magnet through the spin wave.

Figure 2| Experimental setup with a diamond beam and mapping of spin-waves and NV-spin resonance spectra. **a**, Experimental setup for probing thermally excited magnon current via NV centers in a diamond beam centered on the upper YIG's surface. **b**, A schematic toy model of thermal magnon current spin-transfer torque system with a NV spin (dark blue ball with red arrow) and a precessing magnetization \mathbf{M} in YIG (red arrow) under a magnetic field \mathbf{B}_{ext} . The transverse component \mathbf{m} of \mathbf{M} produces an AC magnetic field \mathbf{b}_R that drives the NV spin into its Rabi oscillation. Thermal magnon spin-transfer torque produced by the temperature gradient ∇T is exerted to the \mathbf{M} resulted in the modification of \mathbf{b}_R . \mathbf{M}_s is the saturation magnetization of the YIG. **c**, Microwave-absorption ($P_{\text{MW}} = 1 \text{ mW}$) spin-wave resonance spectra as a function of externally applied magnetic field $+B_{\text{ext}}$ (Solid lines indicate the upper (red, $m_s = 0 \leftrightarrow +1$) and the lower (yellow, $m_s = 0 \leftrightarrow -1$) bounds of possible ground state resonance transition of NV spins). MSSWs are observed at higher frequencies above the Kittel mode (FMR). **d**, ODMR spectra of the NV spins in diamond beam as a function $+B_{\text{ext}}$ field. The region between the two dashed white lines indicates the resonance frequency band of MSSWs. NV1 to NV4 indicate the four possible NV spins directed to $\langle 111 \rangle$ symmetrical axes, as shown in **a**. **e**, Zoomed spin-wave resonance spectra at dotted white square in **c**. Dashed white line indicates

resonance transitions of NV3 spins in **d**, **f**, Zoomed ODMR spectra in dotted white square in **d**, showing a discretized ODMR resonance line of NV3 owing to the crossing with MSSWs' resonant frequencies. **g**, Line cut of **e** at $+B_{\text{ext}} = 19$ mT. **h**, Line cut of **f** at $+B_{\text{ext}} = 19$ mT. Both **g** and **h** show a matching condition at frequency 2.58 GHz.

Figure 3| ODMR spectra and Rabi oscillation frequencies under temperature

differences. **a**, ODMR spectra with various temperature differences ΔT applied to the YIG at $+B_{\text{ext}} = 19$ mT and $P_{\text{MW}} = 1$ mW. ODMR dip contrast evolved monotonically (solid line) with temperature difference ΔT applied to the YIG. **b**, ODMR contrast as a function of temperature difference ΔT applied to the YIG. The error bars were obtained from the standard deviation error of the curve fitting to the data in **b** using a single Lorentzian function (not shown here). **c**, Measurement protocol to excite Rabi oscillation on the NV spins. Laser pulse 1 initializes the NV spins to the $m_s = 0$ state followed by a microwaves pulse with duration τ that drives MSSW in the YIG which then excite the NV spins to the $m_s = -1$ state. Laser pulse 2 probes the remaining NV spins population at the $m_s = 0$ state. τ is varied to produce a stroboscopic oscillation between $m_s = 0$ and $m_s = -1$ states. **d**, Rabi oscillations at three different temperature differences ΔT applied to the YIG for $+B_{\text{ext}} = 19$ mT.

Frequency of Rabi oscillation evolved with applied temperature difference. Colored solid lines are damped sinusoidal function. **e**, Variation in Rabi oscillation frequency $\Omega_R/2\pi$ with temperature difference. **f**, Calculated Rabi field b_R inferred from the Rabi frequency in **e** as a function of applied temperature difference ΔT . **g-i**, Rabi oscillations, Rabi frequencies, and Rabi fields, respectively as a function of temperature difference with $-B_{\text{ext}} = 19$ mT. The error bars in **e**, **f**, **h**, and **i** were obtained from the standard deviation of the curve fitting to the data in **d** and **g**, respectively, with a damped sinusoidal function. Colored solid lines in **e**, **f**, **h** and **i** are fittings to equation (4). Shaded red and blue area in **f** and **i** are the possible variation in the fitting curve based on the uncertainties of the fitting parameters in equation (4) (see Supplementary Note 8).

Figure 4| Local detection of thermal magnon current using a nanodiamond. a,

Experimental setup for local detection of the thermally excited magnon current with a nanodiamond containing several NV spins. **b**, ODMR spectra map of the NV spins in the nanocrystal diamond on the YIG under zero temperature difference ($P_{\text{MW}} = 1$ mW). Non-resonant PL quenching was observed beside the straight lines of the NV spins' resonant transitions $m_s = 0 \leftrightarrow -1$. Inset shows a fluorescence image of the

nanodiamond used in the measurement. **c**, Longitudinal spin relaxation rate measurement protocol to detect the thermally excited magnon current comprising of a polarizing laser pulse followed by a variable duration- τ pulse of the non-resonant NV spin excitation via MSSW at frequency of 2.66 GHz with $\pm B_{\text{ext}} = 13$ mT (dashed black circle in **b**). **d** and **e**, NV spin relaxation rate Γ as a function of temperature difference ΔT applied to the YIG for $+B_{\text{ext}}$ (**d**) and $-B_{\text{ext}}$ (**e**). Solid red line (**d**) and blue line (**e**) are the fitting curve to the data with a model in equation (5). **f**, Measurement protocol for control experiments performed without MSSW driving pulse. **g** and **h**, NV spin relaxation rate Γ shows no dependence on temperature difference ΔT for both positive (**g**) and negative (**h**) external magnetic fields. The error bars in **d**, **e**, **g**, and **h** were obtained from the standard deviation of the curve fitting to the longitudinal spin relaxation data with a single exponential function (see Supplementary Note 5). Shaded red and blue area in **d** and **e** are the possible variation in the fitting curve based on the uncertainties of the fitting parameters in equation (5) (see Supplementary Note 8).

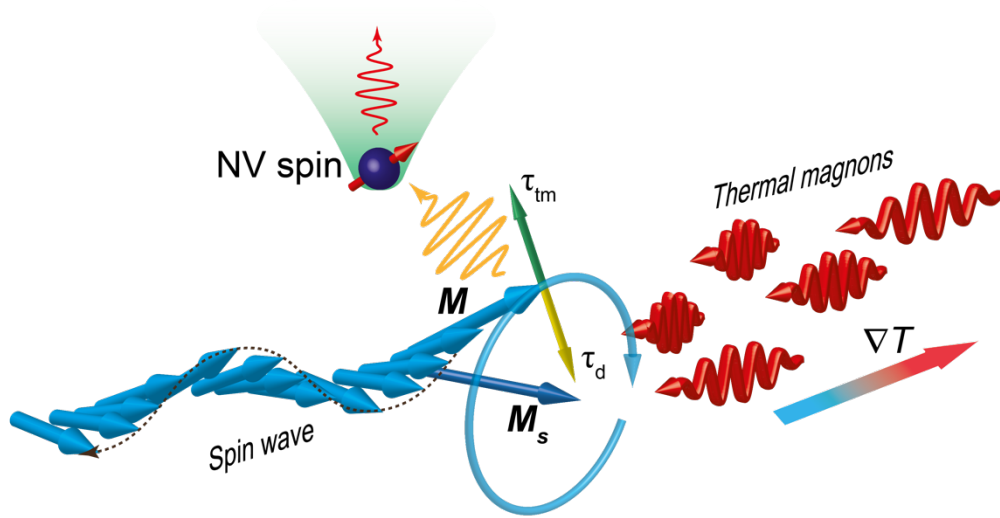


Figure 1.

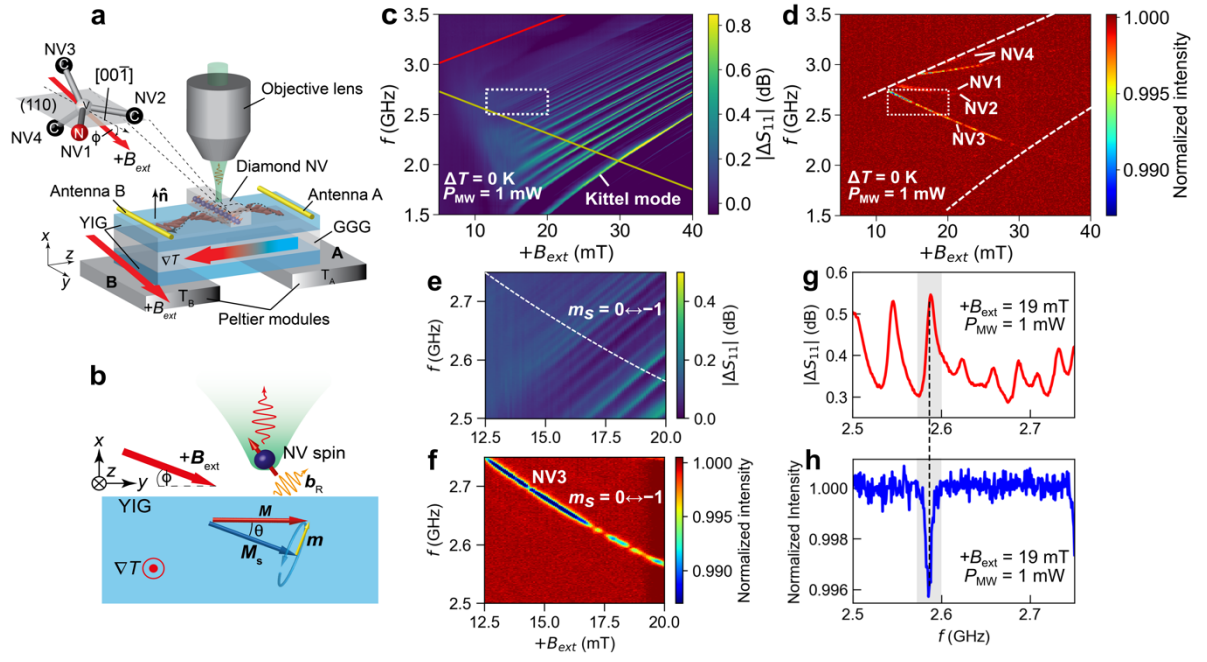


Figure 2.

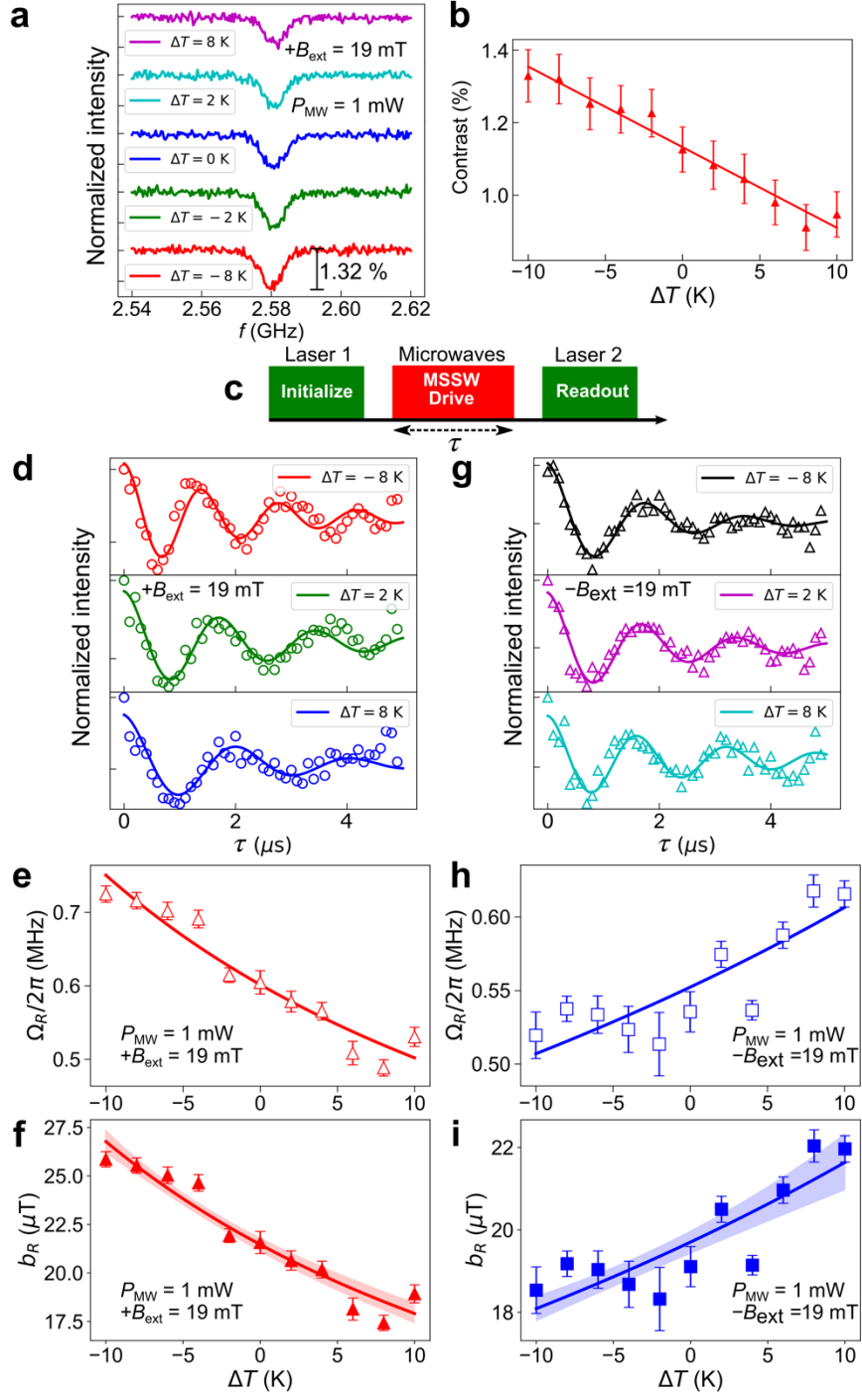


Figure 3.

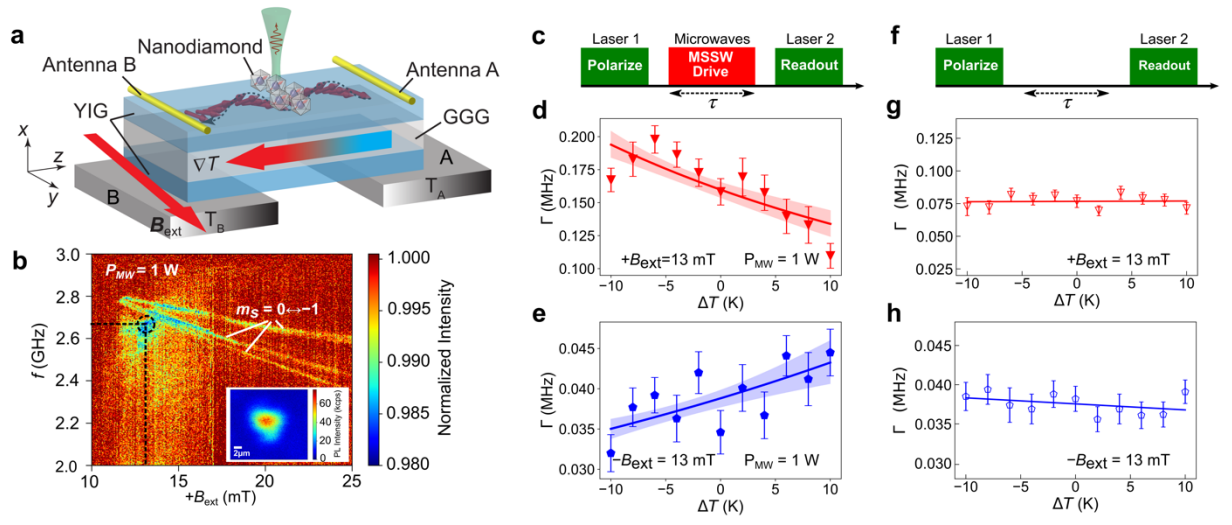


Figure 4.